

**Physical Chemistry Cumulative Exam**  
**Topic: X-Ray Absorption Spectroscopy**

April 2019  
Ksenija Glusac

1. Using 2-3 sentences and/or equations, describe each of the following terms: (a) XANES; (b) EXAFS; (c) core hole; (d) photoelectron; (e) L-edge; (f) synchrotron; (g) Bragg diffraction.
2. Consider a metal center undergoing an L-edge transition from the  $1s^2 2s^2 2p^6 3s^2 3p^6 3d^0$  ground state configuration to the  $1s^2 2s^2 2p^5 3s^2 3p^6 3d^1$  excited-state configuration.
  - (a) Define the atomic term for the ground state configuration. What levels belong to this term?
  - (b) List all atomic terms for the excited-state configurations. What levels belong to each term?
  - (c) Using dipole selection rules, define the excited-state levels to which the X-ray absorption is allowed.
3. The oscillatory features observed in the EXAFS region are described by the photoelectron interference caused by the scattering off the neighboring atoms. Consider a photoelectron formed by the K-edge absorption of X-rays by an atom with the absorption threshold of  $E_0=7.1$  keV. If the photoelectron scatters off an atom that is at the  $R=2.3$  Å distance from the absorbing atom, at what X-ray energies of EXAFS spectrum do you expect to observe the first three constructive interference maxima? Ignore the effects due to multiple neighbor scattering, phase shifts, etc.; consider only the interference due to a single elastic scattering event.
4. Read the attached paper and answer the following questions:
  - (a) Describe briefly (4-5 sentences) the key points of the manuscript: What chemical systems were studied? What property of these samples was investigated? What technique was used? Why was this study performed?
  - (b) What specific absorption edges were used to study holes and electrons in transition metal oxides?
  - (c) How do these measurements report on the covalency of transition metal oxides and their catalytic efficiency toward oxygen evolution reaction?
  - (d) How did the authors distinguish between excitons and charge carriers in their data?
  - (e) What Bohr exciton radii were obtained from the measurements? How does the exciton size correlate with covalency?

Useful constants:

$$m_e=9.1 \cdot 10^{-31} \text{ kg}$$

$$1 \text{ eV}= 1.6 \cdot 10^{-19} \text{ J}$$

$$h=6.63 \cdot 10^{-34} \text{ m}^2\text{kg/s}$$

# Highly Localized Charge Transfer Excitons in Metal Oxide Semiconductors

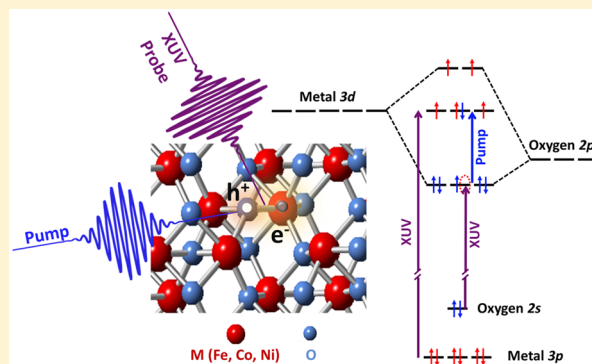
Somnath Biswas,<sup>1</sup> Jakub Husek,<sup>1</sup> Stephen Londo, and L. Robert Baker<sup>\*,1</sup>

Department of Chemistry and Biochemistry, The Ohio State University, Columbus, Ohio 43210, United States

**S** Supporting Information

**ABSTRACT:** The ability to observe charge localization in photocatalytic materials on the ultrafast time scale promises to reveal important correlations between excited state electronic structure and photochemical energy conversion. Of particular interest is the ability to determine hole localization in the hybridized valence band of transition metal oxide semiconductors. Using femtosecond extreme ultraviolet reflection absorption (XUV-RA) spectroscopy we directly observe the formation of photoexcited electrons and holes in  $\text{Fe}_2\text{O}_3$ ,  $\text{Co}_3\text{O}_4$ , and  $\text{NiO}$  occurring within the 100 fs instrument response. In each material, holes localize to the O 2p valence band states as probed at the O  $L_1$ -edge, while electrons localize to metal 3d conduction band states on this same time scale as probed at the metal  $M_{2,3}$ -edge. Chemical shifts at the O  $L_1$ -edge enable unambiguous comparison of metal–oxygen (M–O) bond covalency. Pump flux dependent measurements show that the exciton radius is on the order of a single M–O bond length, revealing a highly localized nature of exciton in each metal oxide studied.

**KEYWORDS:** Covalency, exciton, metal oxides, X-ray absorption, water splitting



First row transition metal oxides have been widely studied as photocatalysts for water oxidation due to their high abundance, electrochemical stability, favorable surface kinetics, and long-lived charge transfer states.<sup>1,2</sup> However, continued improvements in the performance of these materials require a better understanding of the relationship between electronic structure and catalytic activity. Numerous studies have shown that conduction band states are predominantly metal 3d, while valence band electronic structure is more complex, consisting of metal 3d and O 2p states with varying degrees of hybridization.<sup>3,4</sup> While it is agreed that photoexcited electrons in transition metal oxides localize to the metal 3d conduction band states, the localization of photoexcited holes is a subject of continued debate.<sup>5–7</sup> Numerous studies have been performed showing that exact charge carrier localization may depend on a variety of factors, including the specific transition metal cation,<sup>8,9</sup> crystal structure,<sup>10,11</sup> possible dopants,<sup>12,13</sup> presence of surface defects and midgap states,<sup>14,15</sup> and the particle shape.<sup>16</sup> It has additionally been noted that the poor charge carrier mobility of metal oxides limits their overall catalytic efficiency.<sup>7,17</sup> It is well-known that the interaction between the photoexcited electron and hole and the localization dynamics of the resulting exciton are closely related to the charge carrier mobility.<sup>18</sup> Consequently, to fully characterize the excitonic nature of photoexcited states in these metal oxide catalysts, it is critical to understand the localization dynamics of both photoexcited electrons and holes and the nature of the electron–hole pair interaction.

Recent studies have investigated the chemical nature of photoexcited states in the late transition metal oxides  $\text{Fe}_2\text{O}_3$ ,  $\text{Co}_3\text{O}_4$ , and  $\text{NiO}$  using femtosecond XUV spectroscopy.<sup>9,19–21</sup> These studies have shown strong charge transfer character in the photoexcited state by measuring one electron reduction of each of the corresponding metal centers. The measured reduction of the metal centers on the ultrafast (i.e., sub-100 fs) time scale suggests that photoexcitation occurs via an O 2p  $\rightarrow$  metal 3d charge transfer transition. However, to date there has been no report of direct detection of photoexcited holes in metal oxide semiconductors, where the questions of hole localization and valence band hybridization are critical for understanding photoelectrochemical catalysis by these materials.

Although transition metal oxides have complicated band structure, their  $M_{2,3}$ -edge spectra have been well-approximated using ligand field multiplet theory.<sup>8,9,19–21</sup> Figure 1 represents a simplified molecular orbital picture which schematically depicts the basis for detecting a transient hole in the O 2p valence band states using an XUV probe at the O  $L_1$ -edge. In the ground state electronic configuration, O is nominally in the 2–oxidation state dictating a  $2p^6$  electron configuration, and this precludes core-hole excitation to an O 2p orbital. Optically driving a charge transfer excitation results in electron transfer

**Received:** November 14, 2017

**Revised:** January 1, 2018

**Published:** January 25, 2018

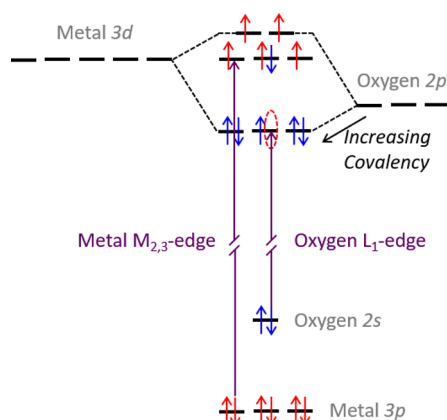


**Figure 1.** In a simplified molecular picture depicting the ground state  $\text{Fe}_2\text{O}_3$ ,  $\text{O}^{2-}$  ligands have a nominal  $2p^6$  electron configuration, which precludes O  $L_1$ -edge absorption. Following a charge transfer photoexcitation, O  $L_1$ -edge absorption is allowed due to the presence of a transient hole on the O  $2p$  states. Similar results are expected for  $\text{Co}_3\text{O}_4$  and  $\text{NiO}$ .

from the O  $2p$  to metal  $3d$  states. The resulting hole in the O  $2p$  valence band is expected to enable a newly allowed dipole transition, which would be observed as an excited state absorption band at the O  $L_1$ -edge in the transient XUV spectrum.

Figure 2 compares the measured transient spectra for (A)  $\text{Fe}_2\text{O}_3$ , (B)  $\text{Co}_3\text{O}_4$ , (C)  $\text{NiO}$ , and (D)  $\text{FeS}_2$  after 2 ps following photoexcitation.  $\text{Fe}_2\text{O}_3$ ,  $\text{Co}_3\text{O}_4$ , and  $\text{FeS}_2$  were photoexcited with 400 nm light, while  $\text{NiO}$  required excitation with 267 nm light due to its larger (i.e.,  $\sim 4$  eV) band gap. In each case, the

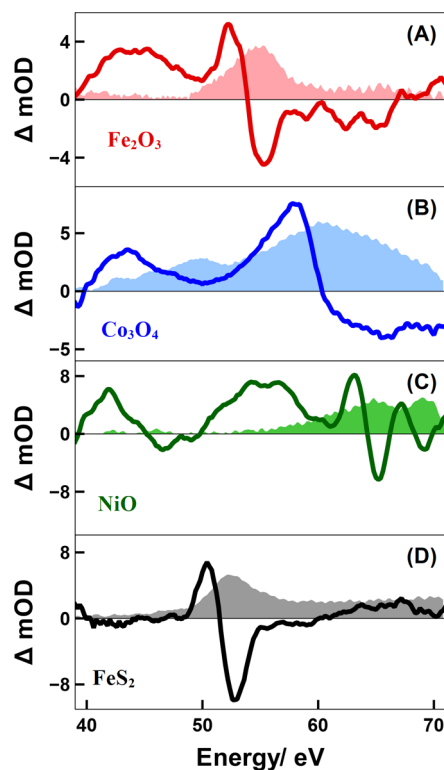


**Figure 2.** Transient XUV-RA spectra of (A)  $\text{Fe}_2\text{O}_3$ , (B)  $\text{Co}_3\text{O}_4$ , (C)  $\text{NiO}$ , and (D)  $\text{FeS}_2$  after 2 ps following photoexcitation. Shaded plots represent the corresponding measured static XUV RA spectra.

ground state spectrum is provided as a shaded background. The shifting transition energies at the metal  $M_{2,3}$ -edges reflects the increased binding energy of the metal  $3p$  core orbitals with increasing atomic number. In the case of  $\text{Fe}_2\text{O}_3$  we observe a bleach of ground state absorption at 55 eV and a corresponding excited state absorption at 53 eV suggesting a loss of  $\text{Fe}^{3+}$  population and an increase in  $\text{Fe}^{2+}$  population. Similar transient line shapes are observed for  $\text{Co}_3\text{O}_4$  and  $\text{NiO}$ . In the case of  $\text{Co}_3\text{O}_4$ , the ground state spectrum is broadened due to the divalent nature of the ground state, which contains both  $\text{Co}^{3+}$  (Oh) and  $\text{Co}^{2+}$  (Td) metal centers.  $\text{NiO}$  actually shows two absorption peaks in the ground state at 65 and 69 eV, which both bleach giving rise to a  $\text{Ni}^+$  absorption band at 63 eV. In each case the exact analysis of the metal  $M_{2,3}$ -edge has been described previously with the use of careful ligand field multiplet calculations.<sup>9,20,21</sup>

Here we also report for the first time the low energy region of the spectrum down to 38 eV. This is the lowest energy we can analyze without interference from second order diffraction of higher energy harmonics. This shows a consistent excited state absorption band centered between 41 and 44 eV for each metal oxide. This energy closely corresponds to 41.6 eV predicted for O  $L_1$ -edge absorption in the Henke tables and is consistent with generation of a transient hole in the O  $2p$  valence band of the photoexcited metal oxides as depicted in Figure 1.<sup>22</sup> To further confirm that this feature is the result of transient hole formation in O  $2p$  valence band states, we compare the spectrum of photoexcited  $\text{FeS}_2$ . Here we observe a similar transient spectrum at the Fe  $M_{2,3}$ -edge as seen in  $\text{Fe}_2\text{O}_3$  indicating transient reduction of the metal center. Importantly, the absence of excited state absorption in the low energy region of the  $\text{FeS}_2$  confirms that this feature can be attributed to O  $L_1$ -edge absorption.

To differentiate between electronic excitations and subsequent thermal effects, the transient response at the metal  $M_{2,3}$ -edge (blue and red) and O  $L_1$ -edges (green) have been plotted in Figure 3C,D for  $\text{Fe}_2\text{O}_3$  and  $\text{NiO}$ , respectively. Chen and co-workers recently reported the appearance of transient signal in the X-ray spectrum of  $\text{Fe}_2\text{O}_3$  due to thermally induced lattice distortions making electronic and thermal spectral contributions difficult to distinguish.<sup>23</sup> However, lattice heating occurs on the order of few to tens of picoseconds based on carrier-phonon scattering times.<sup>24–27</sup> The time resolution for these measurements is  $\sim 100$  fs (approximately 3 orders of magnitude faster than synchrotron-based transient absorption), and we observe the transient spectra form within the instrument response of these measurements. Consequently, we can exclude significant contributions due to thermal effects in our transient signal.

In  $\text{Fe}_2\text{O}_3$  (Figure 3C), the apparent recovery of the transient bleach (blue) at 54 eV occurs with a time constant of 660 fs following photoexcitation. This recovery is correlated with the simultaneous formation of a blue-shifted ground state bleach (red) at 55.2 eV. This ultrafast shift in the position of the ground state bleach is associated with surface trapping of the photoexcited electron and small polaron formation, as has been described in detail recently.<sup>8</sup> In  $\text{NiO}$  (Figure 3D), the ground state bleach at 65 eV (blue) forms within the instrument response and is correlated with the excited state absorption at 63 eV (red). This is a result of  $\text{O}^{2-}(2p) \rightarrow \text{Ni}^{2+}(3d)$  charge transfer transition where  $\text{Ni}^{2+}$  bleaches with the simultaneous formation of  $\text{Ni}^+$ .<sup>21</sup> We do not observe significant decay of the metal  $M_{2,3}$ -edge bleach (red) or O  $L_1$ -edge (green) absorption

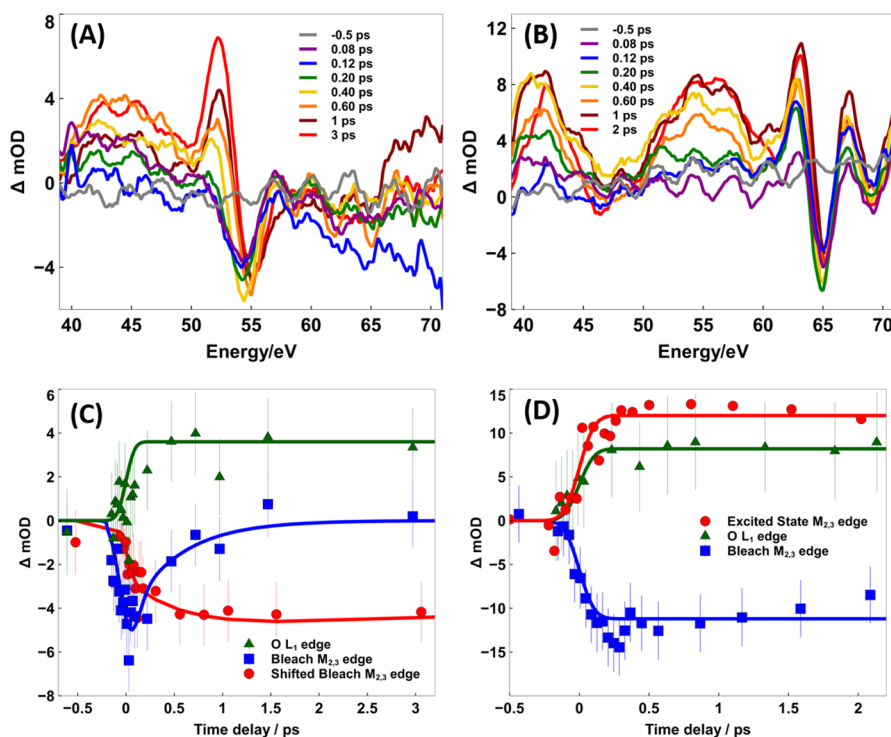


**Figure 3.** Select transient XUV-RA spectra for (A) Fe<sub>2</sub>O<sub>3</sub> and (B) NiO showing the spectral evolution up to  $\sim 3$  ps postexcitation with 400 nm ( $6.2 \text{ mJ}/(\text{pulse cm}^2)$ ) and 267 nm ( $5.3 \text{ mJ}/(\text{pulse cm}^2)$ ) beam, respectively. (C) Transient responses for Fe<sub>2</sub>O<sub>3</sub> at 44 eV (green) associated with the O L<sub>1</sub>-edge transition, at 54.2 eV (blue) associated with the ground state bleaching of the Fe<sup>3+</sup>, and at 55.2 eV (red) associated with the formation of surface trapped polaron. (D) Transient responses of NiO at 41.8 eV (green) associated with O L<sub>1</sub>-edge absorption, 63 eV (red) associated with the absorption of the Ni<sup>2+</sup>, and 65 eV (blue) for the ground state bleach of Ni<sup>2+</sup>. The symbols are experimental data and the solid lines represent the fit. Error bars represent 95% confidence intervals.

in either Fe<sub>2</sub>O<sub>3</sub> or NiO during the first 3 ps after photoexcitation. This suggests that in these studies the electron–hole recombination is occurring on longer time scales as noted previously,<sup>18,28</sup> although some studies have observed carrier recombination in hematite on the fs or even sub-fs time scale.<sup>29</sup> We further observe that the transient kinetics for NiO are independent of pump fluence for time delays up to 3 ps. Figure S3 in the Supporting Information shows results for a lower pump flux of  $1.8 \text{ mJ}/(\text{pulse cm}^2)$  compared to  $5.3 \text{ mJ}/(\text{pulse cm}^2)$  as shown in Figure 3D. Both plots show the appearance of a ground state bleach and excited state absorption within the 100 fs instrument response followed by negligible decay of transient signal within the measured time window. This result suggests that the exciton–exciton interactions do not have a significant influence on the measured kinetics indicating the formation of extremely localized excitons as evident from the discussion below. Additional details of the transient kinetics analysis are found in the Supporting Information.

A number of reports have shown that covalency is an important parameter for understanding the catalytic efficiency of these transition metal oxides.<sup>3–6</sup> For example, a study of 51 metal oxide perovskites utilized a statistical regression analysis to conclude that M–O bond covalency is one of the key indicators of oxygen evolution reaction kinetics.<sup>30</sup> Unfortunately, direct observation of M–O bond hybridization is not straightforward. Ground state X-ray absorption spectroscopy at the O K-edge is indirectly sensitive to M–O bond covalency because it represents a probe of the O 2p character in the unoccupied metal 3d conduction band states. However, correctly interpreting M–O bond covalency from these

measurements requires accurate knowledge of the metal 3d occupancy as well as the relative hybridization of O 2p states with the metal  $e_g$  and  $t_{2g}$  conduction band states making a comparison of covalency difficult, particularly for the late transition metal oxides.<sup>4</sup>

More importantly, ground state X-ray absorption spectroscopy measurements cannot probe the effect of charge transfer excited states on bond hybridization, which is critical for understanding photochemical processes. Direct measurement of excited state chemical shifts in the O 2p states can also probe valence band hybridization, as depicted in Figure 1. The extent of hybridization between the atomic orbitals depends inversely on the energy difference between them. Increased hybridization serves to lower the energy of the O 2p bonding states resulting in a decreased XUV transition energy at the O L<sub>1</sub>-edge due to lowering of the O 2p valence states relative to the O 2s core. The exact position of the O L<sub>1</sub>-edge absorption peak for each metal oxide is given in Table 1. Here we observe that covalency increases with effective nuclear charge such that the L<sub>1</sub>-edge transition is lowest for Ni and highest for Fe. This fits the measured trend for water oxidation kinetics where overpotential decreases from Fe<sub>2</sub>O<sub>3</sub> to Co<sub>3</sub>O<sub>4</sub> to NiO, confirming

**Table 1.** Summary of the Exciton Bohr Radius, M–O Bond Length, Lattice Constant, and O L<sub>1</sub>-Edge Peak Position

	exciton Bohr radius	M–O bond length	lattice constant	oxygen L <sub>1</sub> -edge peak position
Fe <sub>2</sub> O <sub>3</sub>	2.57 Å	2.05 Å	5.04 Å	44 eV
Co <sub>3</sub> O <sub>4</sub>	3.31 Å	1.93 Å	8.07 Å	43 eV
NiO	4.46 Å	2.08 Å	4.18 Å	42 eV



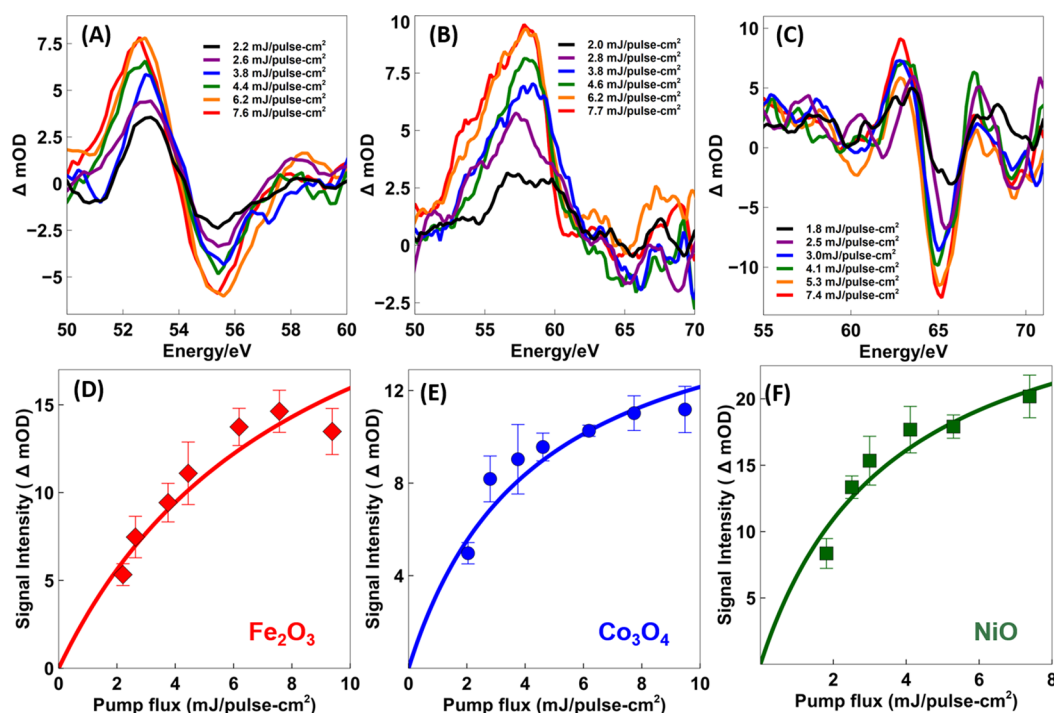


**Figure 4.** Transient RA spectra at the metal  $M_{2,3}$ -edge as a function of pump flux at a fixed time delay of 1.2 ps for (A)  $\text{Fe}_2\text{O}_3$  and 400 fs for (B)  $\text{Co}_3\text{O}_4$ , and (C)  $\text{NiO}$ . (D, E, F) Magnitude of the transient signal intensity as a function of pump flux for  $\text{Fe}_2\text{O}_3$ ,  $\text{Co}_3\text{O}_4$ , and  $\text{NiO}$ , respectively, fitted with the saturable absorber model (solid lines). Error bars represent 95% confidence intervals.

the correlation between M–O covalency and kinetics for these late transition metal oxides.<sup>31</sup>

Figure 4 shows the transient signal intensity at the respective metal  $M_{2,3}$ -edges as a function of pump flux at a fixed time delay of 1.2 ps for (A)  $\text{Fe}_2\text{O}_3$  and 400 fs for (B)  $\text{Co}_3\text{O}_4$ , and (C)  $\text{NiO}$ . The power dependent data at the O  $L_1$ -edge are noisier than at the  $M_{2,3}$ -edges making it difficult to quantify the power dependent trend of transient signal at this energy range, particularly for low pump flux. This is mainly due to the fact that the relative standard deviation of the XUV harmonics is much higher at the low energy side of the spectrum below approximately 50 eV. For this reason, we only report the saturation behavior as a function of pump flux at the respective metal  $M_{2,3}$ -edge. In each case the transient signal shows a characteristic saturation behavior. This saturation behavior at higher pump flux is the result of the exciton–exciton annihilation as described previously.<sup>32,33</sup> Similar nonlinear behavior of the transient signal intensity at the higher pump flux in CdS and CdSe semiconductor nanoparticle systems has also been attributed previously to the exciton–exciton annihilation process.<sup>34</sup> At high exciton density, bimolecular interaction between multiple excitons leads to a rapid electron–hole recombination.<sup>29</sup> Accordingly, a given volume can accommodate a maximum number of excitons, and beyond this limit the transient signal reaches saturation as a result of fast exciton–exciton annihilation. An alternative picture to absorption saturation could be related to a Mott insulator-to-metal phase transition. In this scenario nonlinear transient signal intensity can occur due to the screening of the attractive Coulombic interaction between electron and hole in the presence of high carrier densities. As a result of this, the insulating semiconductor material undergoes a Mott transition to produce highly dense electron–hole plasma. Typically, significant spectral changes are associated with this tran-

sition.<sup>35,36</sup> However, we observe no spectral changes even at the higher excitonic density (Figure 4). Therefore, we exclude the possibility of nonlinear signal saturation due to the Mott transition, and presume a saturable absorber model given by the equation below<sup>37,38</sup>

$$I \propto \frac{\Phi}{\Phi + \Phi_s} \quad (1)$$

where  $I$  represents the transient signal intensity,  $\Phi$  is the pump flux, and  $\Phi_s$  is the saturation flux. The fitted line of the model shows good agreement with the data as shown in Figure 4. The saturation flux (Table 2) from the saturable absorber model enables us to calculate the exciton Bohr radius for each of the metal oxides as describe below.

Equation 2 shows the calculation of exciton Bohr radius where  $V_{\text{XUV}}$  is the probe volume,  $\eta$  is the number of excitons in

**Table 2. Summary of the Calculation for Exciton Bohr Radius**

	metal oxides		
	$\text{Fe}_2\text{O}_3$	$\text{Co}_3\text{O}_4$	$\text{NiO}$
saturation flux (mJ/(pulse $\text{cm}^2$ ))	8.4	4.6	3.7
photons/pulse	$4.13 \times 10^{14}$	$2.23 \times 10^{14}$	$6.04 \times 10^{13}$
extinction coefficient ( $\text{nm}^{-1}$ )	0.034	0.028	0.056
Fresnel factor, $T$	0.97	0.98	0.42
probability of absorption, $P$	0.26	0.22	0.39
number of exciton	$1.03 \times 10^{14}$	$4.81 \times 10^{13}$	$9.92 \times 10^{12}$
volume of an exciton ( $\text{cm}^3$ )	$7.12 \times 10^{-23}$	$1.52 \times 10^{-22}$	$3.72 \times 10^{-22}$
exciton radius (Å)	2.57	3.31	4.46

the probe volume, and  $a_0$  is the exciton Bohr radius. The probe volume is determined by the XUV beam area ( $1.38 \times 10^{-3} \text{ cm}^2$ ) and the measured probe depth ( $\sim 3 \text{ nm}$ ).

$$V_{\text{XUV}} = \eta \frac{4}{3} \pi a_0^3 \quad (2)$$

The value of  $\eta$  can be determined from equation 3 which includes the number of photons per pulse at the saturation flux ( $N$ ), the Fresnel factor ( $T$ ), and the probability of absorption ( $P$ ).

$$\eta = N \times T \times P \quad (3)$$

We calculate the number of photons per pulse ( $N$ ) at the saturation flux of 400 nm pump beam (area =  $2.43 \times 10^{-2} \text{ cm}^2$ ) for  $\text{Fe}_2\text{O}_3$  and  $\text{Co}_3\text{O}_4$ , and 267 nm pump (area =  $1.23 \times 10^{-2} \text{ cm}^2$ ) for NiO from the saturable absorber model. The Fresnel factor and the probability of absorption are obtained from equations 4 and 5, respectively.

$$T = 1 - \left[ \frac{-N^2 \cos(\theta) + \sqrt{N^2 - \sin^2(\theta)}}{N^2 \cos(\theta) + \sqrt{N^2 - \sin^2(\theta)}} \exp\left(\frac{-16\pi^2 R_q^2 \cos^2(\theta)}{3\lambda^2}\right) \right]^2 \quad (4)$$

This is a classical Fresnel equation for the transmittance ( $T$ ) of p-polarized light, corrected by the Debye–Waller factor,<sup>21</sup> where  $\theta$  is the angle of incidence relative to the surface normal ( $\theta = 70^\circ$ ),  $\lambda$  is the wavelength of light, and  $R_q$  is the root-mean-square surface roughness. AFM is used to directly measure  $R_q$ .

$$P = 1 - \exp\left(-\frac{\alpha z}{\cos(\theta)}\right) \quad (5)$$

In this equation  $P$  is the probability of absorption for a pump beam photon,  $\alpha$  is the extinction coefficient of the sample at the pump wavelength, and  $z$  is our measured probe depth ( $\sim 3 \text{ nm}$ ) of the XUV beam.<sup>21</sup> We note that small variations in the value of  $z$  have a negligible effect on the final calculated exciton Bohr radii. The summary of the results and all the parameters are found in Table 2.

The exciton Bohr radii for  $\text{Fe}_2\text{O}_3$ ,  $\text{Co}_3\text{O}_4$ , and NiO are 2.57, 3.31, and 4.46 Å, respectively. Similar exciton Bohr radii of 3 and 13 Å have been reported previously for nanocrystalline films of  $\text{ZnO}$  and  $\text{TiO}_2$ , respectively.<sup>39</sup> These results indicate that the exciton Bohr radii are on the order of the size of the unit cell of these metal oxides. This picture is consistent with the Frenkel exciton model, where excitons represent bound carriers within a single unit cell.<sup>40</sup> This highly localized nature of the exciton is in contrast to nanoscale systems where the delocalized bands facilitate the movement of the electron and hole and is consistent with the low mobility of metal oxide semiconductors.<sup>41,42</sup> We note that similar kinetics of the NiO transient signal are observed both in the saturation regime (Figure 3D) and in the linear regime (Figure S3). This observation further suggests that the excitons in these metal oxides are highly localized and that their size is independent of the pump fluence. Furthermore, we observe a trend in the exciton radii that correlates with the O  $L_1$ -edge peak position of the metal oxides studied here as shown in Table 1. We observe a gradual increase of the exciton radius that corresponds to a bathochromic shift of the O  $L_1$ -edge peak position from  $\text{Fe}_2\text{O}_3$  to  $\text{Co}_3\text{O}_4$  to NiO. We attribute this trend to increased hybridization between metal 3d and O 2p from  $\text{Fe}_2\text{O}_3$  to

$\text{Co}_3\text{O}_4$  to NiO. These results suggest that the excitons tend to delocalize with increasing M–O bond covalency.

In light of the above results, showing hole density primarily in the O 2p valence band states with the electron localized to the metal 3d conduction band states, we conclude that charge separation occurs across essentially a single M–O bond. This study represents the first direct observation of the photo-generated hole directly in the O 2p valence band. Additionally, we show that chemical shifts in the transient O  $L_1$ -edge spectrum are sensitive to M–O bond hybridization enabling us to compare covalency in these late transition metal oxides. Finally, we have measured the size of the exciton using a pump fluence dependent saturable absorber model of the transient signal intensity. These results show that the electron and hole in the charge transfer excited states in each of the metal oxides studied are separated by approximately a single M–O bond length. This study experimentally confirms the highly localized, site-specific nature of photogenerated excitons, and the ability to probe transient kinetics of photoexcited electrons and holes with element specificity will play an important role in understanding the mechanism of photochemical energy conversion in a variety of catalytic systems.

## ■ ASSOCIATED CONTENT

### Supporting Information

The Supporting Information is available free of charge on the ACS Publications website at DOI: 10.1021/acs.nanolett.7b04818.

Sample preparation, detailed experimental procedure for XUV RA spectroscopy, kinetic analysis, sample characterization by XPS and AFM, and transient XUV-RA kinetics of NiO at lower pump fluence (PDF)

## ■ AUTHOR INFORMATION

### Corresponding Author

\*E-mail: baker.2364@osu.edu. Phone: +1 (614) 292-2088.

### ORCID

Somnath Biswas: 0000-0002-5931-4966

Jakub Husek: 0000-0003-4820-462X

L. Robert Baker: 0000-0001-6740-864X

### Notes

The authors declare no competing financial interest.

## ■ ACKNOWLEDGMENTS

This work was supported by Chemical Sciences, Geosciences and Biosciences Division, Office of Basic Energy Sciences, Office of Science, U.S. Department of Energy under DOE Grant DE-SC0014051.

## ■ REFERENCES

- (1) Goodenough, J. B. *Chem. Mater.* **2014**, *26*, 820–829.
- (2) Toroker, M. C.; Carter, E. A. *J. Mater. Chem. A* **2013**, *1*, 2474–2484.
- (3) Greiner, M. T.; Helander, M. G.; Tang, W.-M.; Wang, Z.-B.; Qiu, J.; Lu, Z.-H. *Nat. Mater.* **2012**, *11*, 76–81.
- (4) de Groot, F. M. F.; Grioni, M.; Fuggle, J. C.; Ghijsen, J.; Sawatzky, G. A.; Petersen, H. *Phys. Rev. B: Condens. Matter Mater. Phys.* **1989**, *40*, 5715–5723.
- (5) Ansari, N.; Ulman, K.; Camellone, M. F.; Seriani, N.; Gebauer, R.; Piccinin, S. *Phys. Rev. Materials* **2017**, *1*, 035404.
- (6) Su, Z.; Baskin, J. S.; Zhou, W.; Thomas, J. M.; Zewail, A. H. *J. Am. Chem. Soc.* **2017**, *139*, 4916–4922.

- (7) Liao, P.; Carter, E. A. *J. Phys. Chem. C* **2011**, *115*, 20795–20805.
- (8) Husek, J.; Cirri, A.; Biswas, S.; Baker, L. R. *Chem. Sci.* **2017**, *8*, 8170–8178.
- (9) Jiang, C.-M.; Baker, L. R.; Lucas, J. M.; Vura-Weis, J.; Alivisatos, A. P.; Leone, S. R. *J. Phys. Chem. C* **2014**, *118*, 22774–22784.
- (10) Wang, X.; Kafizas, A.; Li, X.; Moniz, S. J.; Reardon, P. J.; Tang, J.; Parkin, I. P.; Durrant, J. R. *J. Phys. Chem. C* **2015**, *119*, 10439–10447.
- (11) Sachs, M.; Pastor, E.; Kafizas, A.; Durrant, J. R. *J. Phys. Chem. Lett.* **2016**, *7*, 3742–3746.
- (12) Sun, J.; Yang, Y.; Khan, J. I.; Alarousu, E.; Guo, Z.; Zhang, X.; Zhang, Q.; Mohammed, O. F. *ACS Appl. Mater. Interfaces* **2014**, *6*, 10022–10027.
- (13) Rashidi, M.; Burgess, J. A.; Taucer, M.; Achal, R.; Pitters, J. L.; Loth, S.; Wolkow, R. A. *Nat. Commun.* **2016**, *7*, 13258.
- (14) Triggiani, L.; Brunetti, A.; Aloï, A.; Comparelli, R.; Curri, M. L.; Agostiano, A.; Striccoli, M.; Tommasi, R. *J. Phys. Chem. C* **2014**, *118*, 25215–25222.
- (15) Vaida, M. E.; Leone, S. R. *J. Phys. Chem. C* **2016**, *120*, 2769–2776.
- (16) Fitzmorris, B. C.; Patete, J. M.; Smith, J.; Mascorro, X.; Adams, S.; Wong, S. S.; Zhang, J. Z. *ChemSusChem* **2013**, *6*, 1907–1914.
- (17) Linsebigler, A. L.; Lu, G.; Yates, J. T., Jr. *Chem. Rev.* **1995**, *95*, 735–758.
- (18) Cherepy, N. J.; Liston, D. B.; Lovejoy, J. A.; Deng, H.; Zhang, J. Z. *J. Phys. Chem. B* **1998**, *102*, 770–776.
- (19) Carneiro, L. M.; Cushing, S. K.; Liu, C.; Su, Y.; Yang, P.; Alivisatos, A. P.; Leone, S. R. *Nat. Mater.* **2017**, *16*, 819.
- (20) Vura-Weis, J.; Jiang, C.-M.; Liu, C.; Gao, H.; Lucas, J. M.; de Groot, F. M. F.; Yang, P.; Alivisatos, A. P.; Leone, S. R. *J. Phys. Chem. Lett.* **2013**, *4*, 3667–3671.
- (21) Cirri, A.; Husek, J.; Biswas, S.; Baker, L. R. *J. Phys. Chem. C* **2017**, *121*, 15861–15869.
- (22) The Lawrence Berkeley National Laboratory's Center for X-ray Optics: X-ray Interactions with Matter. [http://henke.lbl.gov/optical\\_constants/](http://henke.lbl.gov/optical_constants/) (accessed Mar 18, 2017).
- (23) Hayes, D.; Hadt, R. G.; Emery, J. D.; Cordones, A. A.; Martinson, A. B.; Shelby, M. L.; Fransted, K. A.; Dahlberg, P. D.; Hong, J.; Zhang, X.; et al. *Energy Environ. Sci.* **2016**, *9*, 3754–3769.
- (24) Oum, K.; Lenzer, T.; Scholz, M.; Jung, D. Y.; Sul, O.; Cho, B. J.; Lange, J.; Müller, A. *J. Phys. Chem. C* **2014**, *118*, 6454–6461.
- (25) Winnerl, S.; Orlita, M.; Plochocka, P.; Kossacki, P.; Potemski, M.; Winzer, T.; Malic, E.; Knorr, A.; Sprinkle, M.; Berger, C.; et al. *Phys. Rev. Lett.* **2011**, *107*, 237401.
- (26) Bertoni, R.; Lorenc, M.; Cailleau, H.; Tissot, A.; Laisney, J.; Boillot, M.-L.; Stoleriu, L.; Stancu, A.; Enachescu, C.; Collet, E. *Nat. Mater.* **2016**, *15*, 606–610.
- (27) Clark, J.; Beitra, L.; Xiong, G.; Higginbotham, A.; Fritz, D.; Lemke, H.; Zhu, D.; Chollet, M.; Williams, G.; Messerschmidt, M.; et al. *Science* **2013**, *341*, 56–59.
- (28) Joly, A. G.; Williams, J. R.; Chambers, S. A.; Xiong, G.; Hess, W. P.; Laman, D. M. *J. Appl. Phys.* **2006**, *99*, 053521.
- (29) Pendlebury, S. R.; Wang, X.; Le Formal, F.; Cornuz, M.; Kafizas, A.; Tilley, S. D.; Gratzel, M.; Durrant, J. R. *J. Am. Chem. Soc.* **2014**, *136*, 9854–9857.
- (30) Hong, W. T.; Welsch, R. E.; Shao-Horn, Y. *J. Phys. Chem. C* **2016**, *120*, 78–86.
- (31) McCrory, C. C.; Jung, S.; Ferrer, I. M.; Chatman, S. M.; Peters, J. C.; Jaramillo, T. F. *J. Am. Chem. Soc.* **2015**, *137*, 4347–4357.
- (32) Chmeliov, J.; Narkeliunas, J.; Graham, M. W.; Fleming, G. R.; Valkunas, L. *Nanoscale* **2016**, *8*, 1618–1626.
- (33) Sun, D.; Rao, Y.; Reider, G. A.; Chen, G.; You, Y.; Brézin, L.; Harutyunyan, A. R.; Heinz, T. F. *Nano Lett.* **2014**, *14*, 5625–5629.
- (34) Zhang, J. Z. *J. Phys. Chem. B* **2000**, *104*, 7239–7253.
- (35) Chernikov, A.; Ruppert, C.; Hill, H. M.; Rigosi, A. F.; Heinz, T. F. *Nat. Photonics* **2015**, *9*, 466–470.
- (36) Gao, S.; Liang, Y.; Spataru, C. D.; Yang, L. *Nano Lett.* **2016**, *16*, 5568–5573.
- (37) Cunningham, P. D.; McCreary, K. M.; Jonker, B. T. *J. Phys. Chem. Lett.* **2016**, *7*, 5242–5246.
- (38) Kumar, N.; Cui, Q.; Ceballos, F.; He, D.; Wang, Y.; Zhao, H. *Phys. Rev. B: Condens. Matter Mater. Phys.* **2014**, *89*, 125427.
- (39) Enright, B.; Fitzmaurice, D. *J. Phys. Chem.* **1996**, *100*, 1027–1035.
- (40) Scholes, G. D.; Rumbles, G. *Nat. Mater.* **2006**, *5*, 683–696.
- (41) Morin, F. *Phys. Rev.* **1954**, *93*, 1199.
- (42) Morin, F. *Phys. Rev.* **1954**, *93*, 1195.